Blanching Defects at the Pressure Points: Observations from Dynamic Total-Body PET/CT Studies

Running title:

Blanching Defects at the Pressure Points

Authors:

Yasser G. Abdelhafez[1,2], Kristin McBride[1], Edwin K. Leung[1,3,4], Heather Hunt[1], Benjamin A. Spencer[1], Javier E. Lopez[5,6], Kwame Atsina[5,6], Elizabeth J. Li[3], Guobao Wang[1], Simon R. Cherry[1,3], Ramsey D. Badawi[1,3], Fatma Sen[1], Lorenzo Nardo[1]

Affiliations:

[1]Department of Radiology, [3]Biomedical Engineering, [5]Internal Medicine, and [6]Cardiovascular Research Institute, University of California Davis, Davis, CA, USA; [2] Nuclear Medicine Unit, South Egypt Cancer Institute, Assiut University, Egypt; [4] UIH America, Inc., TX, USA

First and Corresponding author: Yasser G. Abdelhafez, M.D., Ph.D., Department of Radiology, University of California, Davis, 3195 Folsom Blvd, EXPLORER Molecular Imaging Center, Sacramento, CA 95816, USA, Phone: (916) 731-9004, Fax: (916) 451-0119, E-mail: yabdelhafez@ucdavis.edu

Word count: 5474

Figures: 4

Tables: 3

ABSTRACT

Total-body PET/CT allows simultaneous acquisition of all the body parts in a single bed position during the radiotracer uptake phase. Dynamic imaging protocols employing total-body PET could demonstrate findings that may not have been previously visualized or described using conventional PET/CT scanners. We examined the characteristics of blanching defects, areas of markedly reduced (partial defect) or absent (complete defect) radiotracer uptake seen at the skin/subcutaneous tissues opposite the bony prominences at pressure points.

Methods

In this observational study, 77 participants underwent dynamic total-body PET/CT imaging using ^{18}F-FDG (Group 1, N=47, 60-min dynamic, arms-down, divided into 3 subgroups according to the injected dose) or ^{18}F-fluciclovine (Group 2, N=30, 25-min dynamic, arms above the head). 40 out of 47 participants in Group 1 were re-imaged at 90 min after being allowed off the scanning table. Blanching defects, partial or complete, were characterized opposite the bony prominences at 7 pressure points (the skull, scapula, and calcaneus bilaterally, as well as the sacrum). Association of the blanching defects with different clinical and technical characteristics were analyzed using uni- and multi-variate analyses.

Results

A total of 124 blanching defects were seen in 68 out of 77 (88%) participants at one or more pressure points. Blanching defects were higher, on average, in Group 2 participants (3.5±1.7) compared to Group 1 (2.1±1.4; P <0.001), but it did not vary within Group 1 for

different ^{18}F-FDG dose subgroups. All defects resumed normal pattern on delayed static (90-min) images except for 14 partial defects. No complete blanching defects were seen on the 90-min images. By multivariate analysis, arm positioning above the head was associated with skull defects; scapular and sacral defects were significantly more encountered in men and with lower BMI, while calcaneal defects could not be associated to any factor.

Conclusion

Blanching defects opposite the bony pressure points are common on dynamic total-body PET/CT images using different radiopharmaceuticals and injection doses. Their appearance should not be immediately interpreted as an abnormality. The current findings warrant further exploration in a prospective setting and may be utilized to study various mechano-pathologic conditions, such as pressure ulcers.

Key Words: total-body PET/CT; dynamic scans; pressure points; blanching defects; skin and subcutaneous tissue

INTRODUCTION

Total-body PET/CT has recently been implemented in both research and clinical fields (*1,2*). The uEXPLORER total-body PET/CT scanner's long axial field-of-view (FOV) of 194 cm not only allows for simultaneous acquisition of radiotracer kinetics across the entire body but also improves the signal collection efficiency, which, coupled with high spatial resolution, results in high-resolution and high-quality images (*3*). For the first time, it is now possible to obtain high-quality total-body dynamic images, which can be used in both research and in the clinic (*4*). In the research field, total-body dynamic imaging has been described and is useful for, for example, obtaining biomarkers characterizing the delivery and uptake of FDG (e.g., K_1 and K_i) via kinetic modeling (*5–9*). In the clinical field, dynamic imaging has been suggested by different groups for a variety of applications. For example, in the imaging of prostate cancer, dynamic imaging helps tumor detection and characterization, especially in the pelvis (*10–12*). Several guidelines have incorporated dynamic acquisitions as part of their recommended imaging protocols (*13–17*). However, the implementation of high-resolution and high-quality total-body acquisitions may enhance the prominence of additional findings that have not been previously described in the literature.

In this work, we characterized, for the first time, the presence of markedly reduced or absent radiotracer uptake seen at the skin/subcutaneous tissues opposite the bony prominences at pressure points, described hereafter as blanching defects, which were noted on dynamic total-body PET images performed with ^{18}F-FDG or ^{18}F-fluciclovine.

MATERIALS AND METHODS

Study Participants

This is a retrospective review of 4 prospectively acquired, IRB-approved studies for other research purposes (#1341792, #1374902, #1470016, and #1480948). All participants provided written informed consent prior to being scanned. The participants were divided according to the injected tracer into two groups: Group 1 (^{18}F-FDG) included 47 participants under 3 sub-groups according to the injected radiotracer dose (Table 1). Group 2 (^{18}F-fluciclovine) included 30 men with prostate cancer who were referred for a standard-of-care evaluation using ^{18}F-fluciclovine total-body PET/CT.

Total-Body PET/CT Scanning

All participants underwent list-mode dynamic PET/CT acquisition, as part of their respective study protocol, on a total-body PET/CT scanner (uEXPLORER, United Imaging Healthcare). The scanner (*3*) has an axial FOV of 194 cm, PET spatial resolution of ≤3.0 mm in full width at half maximum near the center of axial FOV, and an 80-detector row CT with a minimum slice thickness of 0.5 mm. Prior to the acquisition of dynamic PET data, a low-dose (tube current: ~50 mA) or ultra-low-dose (tube current: ~5 mA) CT scan (both with a tube voltage of 140 kVp) was acquired for attenuation correction and anatomical localization. The tube current was automatically modulated by the scanner manufacturer's algorithm.

All PET data were acquired in a list-mode data format, with the participants in the supine position. Positioning aids were provided according to participant's comfort level. For

Group 1, all participants were positioned with arms down and underwent dynamic, 60-min acquisitions, starting at the time of IV injection of ^{18}F-FDG dose ranging from 17.2 MBq to 393.8 MBq (dose groups are summarized in Table 1). The last 20 min of acquisition (40 – 60 min after injection) were reconstructed into a single frame for the purpose of reviewing. According to their respective protocols, 40 out of 47 participants in Group 1 were re-imaged for 20 min starting at 90-min post-injection (i.e., ~30 min after the end of the dynamic acquisition). Participants were allowed to get off the scanner table between scans and empty their urinary bladder. The second scan was used to assess the changes within the blanching defects noted on the first set of images (the dynamic acquisition). Seven participants in Group 1, all with cancer, had a follow-up dynamic scan after a median of 16 days (range: 14-24) for other research purposes. These follow-up scans were utilized to monitor the stability of the distribution of blanching defects.

For Group 2, arms were positioned above the head in 29 out of 30, and to the side in a single subject. PET images were acquired for a total of 25 min, starting immediately after injection of 314.6±19.7 (range: 287.2-389.6) MBq of ^{18}F-fluciclovine. The PET data were reconstructed into 10-min time frames, including 4 – 14 min and 15 – 25 min frames for the purpose of reviewing.

All images were reconstructed using the vendor's software, which utilizes a time-of-flight, ordered subset expectation maximization algorithm, with 4 iterations and 20 subsets. Attenuation-corrected (AC) and non-attenuation corrected (NAC) images were generated for analysis. All PET corrections were applied to the AC images (scatter, randoms, dead-time and normalization). No point-spread function modeling or post-reconstruction smoothing was applied. The reconstruction matrix size was 256 x 256, generating 2.344

mm isotropic voxels. The described reconstruction parameters are the same used for the routine clinical readouts (*1,2*).

PET/CT Image Analysis

The reconstructed PET/CT images were transferred to an image viewing workstation running OsiriX MD 12.0 (Pixmeo, Bernex, Switzerland), and reviewed independently by two nuclear medicine physicians (5 and 13 years of PET/CT experience post-training, respectively). Agreement between the two readers was considered the final reading. For discordant readings, a third nuclear medicine physician (20 years of experience) was consulted, blinded to prior readings, and the final decision was considered based on the agreement of any two readers.

Both AC and NAC images were reviewed side-by-side for any skin/subcutaneous areas of complete (Grade 2) or partial (Grade 1) absence of the expected normal radiotracer uptake (Grade 0) compared to the surrounding tissues at different pressure points. Figure 1 illustrates examples of partial and complete defects. The pressure points were defined as the anatomical locations where a bony structure could restrict blood flow to the overlying tissues due to patient positioning or weight burden. For the current analysis, 4 locations, named after their bony prominences, were studied: skull, scapulae, sacrum, and calcaneus. Except for the sacrum, laterality was also noted as right, left, or bilateral. In the presence of bilateral defects with different defect grades, the higher grade was recorded for that pressure point.

For participants who had additional static scans at 90-min post-injection, the images were read after recording the impression from the dynamic dataset.

Fused PET/CT images were reviewed for any visual gross misregistration between PET and CT at the pressure points as well as for the presence of any anatomical abnormality in the studied pressure points (e.g., skin ulceration or masses). The CT window level was adjusted to identify and precisely locate the different positioning aids (e.g., back or knee cushions) on the CT images (Figure 1).

Statistical Analysis

Differences in continuous data (e.g., age, body-mass index [BMI]) were compared between the two primary groups (with and without blanching defects) using the independent samples T-test for normally distributed data, and Mann-Whitney U test for non-normally distributed data. Differences in qualitative features were compared using the chi-squared test or the Fisher's exact test, as appropriate. Both participant- and site-based analyses were performed. A participant with a blanching defect at one or more site(s) was considered positive for blanching defects. Individual factors that showed some association with the presence of blanching defects ($P<0.05$) in univariate analysis (UVA) were further analyzed using multivariate analysis (MVA) employing binary logistic regression. All models were adjusted for age, sex, injected dose, and BMI, in addition to the interactions between correlated variables (e.g., arm position and tracer group) as appropriate.

Agreement between the two primary readers on the total count of blanching defects per participant was compared using intraclass correlation coefficient (ICC). Agreement on the qualitative evaluation (i.e., the presence or absence of blanching defects, laterality, and grade) was compared using Cohen's kappa analysis.

RESULTS

Study Participants

The general characteristics of the study population are given in Table 1. Group 1 (^{18}F-FDG) included 18 females, 29 males with a mean age of 51.2±13.2 yrs (range: 26.0-78.0). Compared to Group 1, Group 2 participants were all men (P<0.001), older (71.0 ±8.3 vs. 51.2 ±13.3 yrs, P<0.001), taller (178.1±7.8 vs. 171.8±9.8 cm, P=0.002), and marginally heavier (91.0±16.7 vs. 83.5±16.9 kg, P=0.06); however, their mean BMI was comparable to Group 1. The groups had comparable setups regarding the positioning aids (namely, the use of knee and back cushions). A head support was used in all participants.

Of the 77 participants, 37 had cancer (30 prostate and 7 with urothelial tumors), 10 had cardiovascular disease (CVD; with history of recent myocardial infarction), while the remaining 30 were healthy participants not known to have had recent myocardial infarction or cancer.

Agreement Analysis

There was no significant difference in the number of reported blanching defects per participant between the two readers (2.5±1.8 vs. 2.6±1.6, P=0.5), with ICC of 0.90 (95% CI: 0.85-0.94). Also, there was moderate to substantial agreement (range: 0.66-0.88) on

reporting the blanching defect laterality and grade, both on participant- and site-bases (Table 2).

Characteristics of the Blanching Defects

All encountered blanching defects from both groups were seen in both AC and NAC images. On the final reading, a total of 124 blanching defects were seen in 68 out of 77 (88%) participants at one or more pressure points.

The average number of defects was higher in Group 2 participants (3.5±1.7) compared to Group 1 (2.1±1.4; P <0.001) but did not vary within Group 1 for different ^{18}F-FDG dose subgroups. On average, 2.2±1.3, 2.0±1.6, and 2.1±1.5 defects were observed per participant in low-, intermediate-, and standard-dose groups, respectively (P=0.8).

Blanching defects against the scapulae and calcaneus on dynamic imaging were the most frequent and tended to be bilateral and complete defects (Table 3). Only 14 partial defects from 9 participants were still seen on the delayed static (90-min post-injection) images (Figure 2). No complete blanching defects were seen on the 90-min images. The distribution of the blanching defects is summarized in Table 3. Among the 7 participants that had follow-up dynamic scanning, a total of 6 defects were encountered at baseline compared to 8 in the follow-up scans. The distribution, laterality, and grade changed between the two scans within the same participant. For example, one participant who previously showed bilateral complete defects opposite the calcaneus, demonstrated only unilateral partial calcaneal defect on the repeated scan (Figure 3).

It is worth noting that blanching defects beyond the above-described pressure points were not systematically evaluated; however, we noticed variable degrees of blanching defects

at other sites where bony parts press against a tightened or hard structure; for example, prominent spinous processes at the cervico-dorsal region at the site of transition between the head support and the scanner table; elbows against the scanning table or immobilization belts; distal parts of the legs against the end of knee cushions when the heels are not touching the scanning table; and the forefeet against the tightened immobilization aids **(Figure 4).**

Factors Associated with the Presence of Blanching Defects

On a participant-basis, the presence or absence of blanching defects on dynamic scans did not vary according to age, sex, height, weight, BMI, injected dose, fasting hours, or blood glucose level. Also, the use of cushions (back and/or knee), or misregistration between the PET and CT were not associated with these defects. 29 out of 30 participants in Group 2 had their arms up and showed one or more defects compared to 39 out of 47 with arms to the side (P=0.01).

On a site-basis (Supplementary Table S1), the clinical and scan features associated with the presence of blanching defects varied according to the anatomical site. On UVA, both skull and scapular defects were seen more frequently in Group 2 participants (older participants who were scanned with their arms up). Furthermore, scapular defects were significantly more often encountered in taller males. However, in MVA, only arm positioning above the head was associated with skull defects (OR: 11.5; 95% CI: 3.7-35.7; P<0.001) while scapular and sacral defects were associated with lower BMI and male sex. Defects around the calcaneus were not associated with any of the studied characteristics.

The use of back or knee cushions did not significantly affect the frequency or distribution of these defects. However, back pillows were used in only 4 participants. Knee cushions, on the other hand, were used for most participants; nevertheless, they were not associated with the presence of defects opposite the calcaneus.

DISCUSSION

In this report we showed, for the first time, that dynamic total-body PET/CT imaging frequently demonstrated multiple areas of absent or markedly diminished radiotracer uptake against the pressure points. These areas included the sides of the scalp, being pressed against the parietal bones, and the skin and subcutaneous tissues opposite the bony prominences of scapulae, sacrum, and calcaneus.

We hypothesize that these defects may be related to the absence of decreased perfusion induced by mechanical compression, or displacement of the blood within the micro-circulation at the pressure sites near the bony prominence, where the skin/subcutaneous tissue is known to be thinned out and the pressure is high (*18*). This was supported by several findings: 1) the defects followed a close anatomical distribution and photopenic patterns regardless of the mechanism of uptake of the tracer; 2) the defects improved or resolved on delayed imaging, when the participants were allowed to walk freely and return to the same scanning position; 3) the lack of any anatomical correlations from the CT images at these sites (e.g., skin discontinuity, ulceration, or necrotic masses). Though dynamic PET acquisition has been well-established, especially for brain imaging, the current observation has not previously described. This could be explained, at least

partially, by the outstanding gain in scanner sensitivity, which made subtle observations far more obvious than with conventional scanners.

Although most PET/CT imaging centers use simplified static approaches in the clinical setting, dynamic acquisition protocols are increasingly included in several guidelines (*13–17*). Therefore, identification and characterization of these blanching defects may have both clinical and research relevance. This is particularly relevant for the interpretation of routine ^{18}F-fluciclovine scans. ^{18}F-fluciclovine PET/CT imaging guidelines (*16*) recommend early scanning around 3-5 min post-injection (with the dynamic acquisition protocol being optional). Accordingly, most institutions inject the tracer while the patient is lying on the scanner table, then begin the PET data acquisition either immediately or at around the 4th min post-injection, starting at the pelvis and moving cranially. It is worth noting that this protocol is primarily acquired with the arms above the head. This position leads to scapular rotation upward and may also increase the tension on the posterior paraspinal cervical muscles, thereby adding more pressure on the skull. In our data, the scalp and scapular defects were encountered more frequently in Group 2 participants.

In our work, 40 participants underwent delayed static imaging 30 min after the end of a 60-min dynamic PET acquisition. In 31 of them, the uptake was normalized at the pressure points. We assume that the resumption of the tracer delivery and uptake, after prolonged cessation of circulation at these pressure points, may be partially explained by a mechanism close to the "tourniquet effect" (*19*), where prolonged pressure may cause temporary local decrease in perfusion and subsequent compensatory vasodilation after release of the pressure, re-delivering part of the circulating tracer in the blood pool to the sites with defects. Only 9 participants continued to demonstrate partial defect(s) at one or

more pressure points (Table 3). We hypothesize that the magnitude of pressure (in terms of force and duration) may be related to the rate of resumption of the circulation at these points and may vary under different physiologic and pathologic conditions. This hypothesis may be clinically relevant for assessment of cutaneous microvascular circulation. Currently, capillary refill time (CRT) test is commonly used as a simple means for assessment of macrovascular disease and cutaneous perfusion (*20*). In this test, the examiner applies firm external pressure by a finger to the distal phalanx of a finger or toe, and the time required to recover the normal skin color is recorded. The test, though simple and widely used, is not standardized regarding the magnitude/duration of the applied pressure, cut-off for abnormality, or interpretation criteria. Also, it lacks sensitivity and reliability with wide inter- and intra-observer variability (*21*). Accordingly, many other methods for assessing the peripheral perfusion has been introduced (*22*). The highly sensitive total-body PET scanners can capture and quantify radiotracer dynamic processes as they occur in real time, simultaneously with other organs and tissue kinetics (*7,8,23*) and may be utilized towards studying different mechano-pathological conditions, such as pressure ulcers. These possibilities warrant further exploration in a prospective setting.

Finally, we note some limitations of the current report. Although the data were prospectively collected in the context of other projects, this report was generated based on retrospective serendipitous evaluation of these scans, and accordingly, potential clinical characteristics and additional tests that might relate to the current finding were not collected. For example, scapular and sacral defects were encountered more frequently in men with lower BMI, which might indicate that sex differences, hormonal status, and fat

volume could attribute to the finding. Also, local skin conditions that could have been appreciated with direct inspection, Raynaud phenomenon, or autoimmune diseases were not captured in this report. The micro-circulation is tightly controlled under numerous external and internal pathophysiologic mechanisms, and the current work cannot provide further direct clinical implications of the described findings. Also, due to the retrospective nature of our study, we could not demonstrate a clear association to the positioning setup of the participants, which could be far more complex than mere descriptions under body build, cushion location, type, geometry, or any other characteristics of positioning aids. Additionally, we limited our results to seven pressure points, while in realty few other blanching defects could be encountered (Figure 4). The sporadic nature of these defects prevents accurate systematic evaluation. Furthermore, the position of the arms was tightly linked to the tracer group. Although we compensated for the interaction term between these two variables, we believe that having participants with arms up and down homogeneously distributed in each tracer group would be preferable. Another limitation is the relatively high frequency of misregistration between the PET and CT components of the images. In a total-body scanner, the whole body is covered within the field of view during the whole acquisition duration; accordingly, any as motion in one region of the body could affect the attenuation correction and scatter correction in other regions (*2*). With the high sensitivity of total-body PET, data-driven motion compensation techniques could be explored as a potential solution (*24*).

CONCLUSION

Blanching defects opposite the pressure points are common on dynamic total-body PET/CT imaging using the uEXPLORER scanner with different radiopharmaceuticals and

injection doses. Their appearance should not be immediately interpreted as an abnormality. The changes in tracer distribution taking place at the pressure points across the body can be captured in real time on the high-sensitivity total-body PET/CT scanner and can be leveraged in a prospective setting to study various circulatory changes occurring in different mechano-pathologic conditions such as pressure ulcers.

DISCLOSURE

ACKNOWLEDGEMENTS

KEY POINTS

QUESTION:

Are there any unusual findings seen opposite the pressure points on dynamic total-body PET imaging?

PERTINENT FINDINGS:

In this observational study, we included 77 participants who underwent dynamic total-body PET/CT imaging using ^{18}F-FDG (N=47) or ^{18}F-fluciclovine (N=30). Blanching defects, described as areas with markedly decreased or completely absent radiotracer uptake in the skin/subcutaneous tissue at the pressure points opposite the skull, scapulae, sacrum, and calcaneus, were seen in 39 out of 47 (^{18}F-FDG) and 29 out of 30 (^{18}F-fluciclovine) total-body dynamic scans.

IMPLICATIONS FOR PATIENT CARE:

Blanching defects are commonly encountered on dynamic total-body PET imaging with both ^{18}F-FDG or ^{18}F-fluciclovine and should not be mistaken for any abnormality.

REFERENCES

1. Nardo L, Abdelhafez YG, Spencer BA, Badawi RD. Clinical Implementation of Total-Body PET/CT at University of California, Davis. *PET Clin*. 2021;16:1-7.

2. Kwan Q, Ng T, Katherine E, et al. Total-body PET/CT – first clinical experiences and future perspectives. *Semin Nucl Med*. March 2022.

3. Spencer BA, Berg E, Schmall JP, et al. Performance Evaluation of the uEXPLORER Total-Body PET/CT Scanner Based on NEMA NU 2-2018 with Additional Tests to Characterize PET Scanners with a Long Axial Field of View. *J Nucl Med*. 2021;62:861-870.

4. Badawi RD, Shi H, Hu P, et al. First Human Imaging Studies with the EXPLORER Total-Body PET Scanner. *J Nucl Med*. 2019;60:299-303.

5. Wang G, Nardo L, Parikh M, et al. Total-Body PET Multiparametric Imaging of Cancer Using a Voxel-wise Strategy of Compartmental Modeling. *J Nucl Med*. November 2021:jnumed.121.262668.

6. Liu G, Hu P, Yu H, et al. Ultra-low-activity total-body dynamic PET imaging allows equal performance to full-activity PET imaging for investigating kinetic metrics of 18F-FDG in healthy volunteers. *Eur J Nucl Med Mol Imaging*. 2021.

7. Wu Y, Feng T, Zhao Y, et al. Whole-body Parametric Imaging of FDG PET using uEXPLORER with Reduced Scan Time. *J Nucl Med*. August 2021:jnumed.120.261651.

8. Feng T, Zhao Y, Shi H, et al. Total-Body Quantitative Parametric Imaging of Early

Kinetics of 18F-FDG. *J Nucl Med*. 2021;62:738-744.

9. Sarkar S, Matsukuma KE, Spencer B, et al. Dynamic Positron Emission Tomography/Computed Tomography Imaging Correlate of Nonalcoholic Steatohepatitis. *Clin Gastroenterol Hepatol*. 2021;19:2441-2443.

10. Turkbey B, Mena E, Shih J, et al. Localized Prostate Cancer Detection with 18F FACBC PET/CT: Comparison with MR Imaging and Histopathologic Analysis. *Radiology*. 2014;270:849.

11. Tulipan AJ, Vlatkovic L, Malinen E, et al. Comparison of time curves from dynamic 18F-fluciclovine positron emission tomography and dynamic contrast-enhanced magnetic resonance imaging for primary prostate carcinomas. *Phys Imaging Radiat Oncol*. 2018;7:51.

12. Uprimny C, Kroiss AS, Decristoforo C, et al. Early dynamic imaging in 68 Ga-PSMA-11 PET/CT allows discrimination of urinary bladder activity and prostate cancer lesions. *Eur J Nucl Med Mol Imaging*. 2017;44:765-775.

13. Morbelli S, Esposito G, Arbizu J, et al. EANM practice guideline/SNMMI procedure standard for dopaminergic imaging in Parkinsonian syndromes 1.0. *Eur J Nucl Med Mol Imaging 2020 478*. 2020;47:1885-1912.

14. Law I, Albert NL, Arbizu J, et al. Joint EANM/EANO/RANO practice guidelines/SNMMI procedure standards for imaging of gliomas using PET with radiolabelled amino acids and [18 F]FDG: version 1.0. *Eur J Nucl Med Mol Imaging*. 2019;46:540-557.

15. Sciagrà R, Lubberink M, Hyafil F, et al. EANM procedural guidelines for PET/CT

quantitative myocardial perfusion imaging. *Eur J Nucl Med Mol Imaging*. 2021;48:1040-1069.

16. Nanni C, Zanoni L, Bach-Gansmo T, et al. [18F]Fluciclovine PET/CT: joint EANM and SNMMI procedure guideline for prostate cancer imaging—version 1.0. *Eur J Nucl Med Mol Imaging*. 2020;47:579-591.

17. Varrone A, Asenbaum S, Vander Borght T, et al. EANM procedure guidelines for PET brain imaging using [18F]FDG, version 2. *Eur J Nucl Med Mol Imaging*. 2009;36:2103-2110.

18. Cichowitz A, Pan WR, Ashton M. The heel: Anatomy, blood supply, and the pathophysiology of pressure ulcers. *Ann Plast Surg*. 2009;62:423-429.

19. Desaia A, Intenzo C. The "tourniquet effect". *J Nucl Med*. 1984;25:697-9.

20. Fleming S, Gill P, Jones C, et al. The Diagnostic Value of Capillary Refill Time for Detecting Serious Illness in Children: A Systematic Review and Meta-Analysis. *PLoS One*. 2015;10:e0138155.

21. Pickard A, Karlen W, Ansermino JM. Capillary refill time: Is it still a useful clinical sign? *Anesth Analg*. 2011;113:120-123.

22. Liu C, Correia R, Ballaji H, Korposh S, Hayes-gill B, Morgan S. Optical Fibre Sensor for Simultaneous Measurement of Capillary Refill Time and Contact Pressure. *Sensors 2020, Vol 20, Page 1388*. 2020;20:1388.

23. Qi J, Matej S, Wang G, Zhang X. 3D/4D Reconstruction and Quantitative Total Body Imaging. *PET Clin*. 2021;16:41-54.

24. Berg E, Revilla EM, Abdelhafez YG, et al. Framework design for comprehensive

patient motion compensation in total-body PET. Virtual 2020 IEEE Nuclear

Science Symposium & Medical Imaging Conference.

https://www.eventclass.org/contxt_ieee2020/online-program/session?s=M-10.

FIGURE 1:
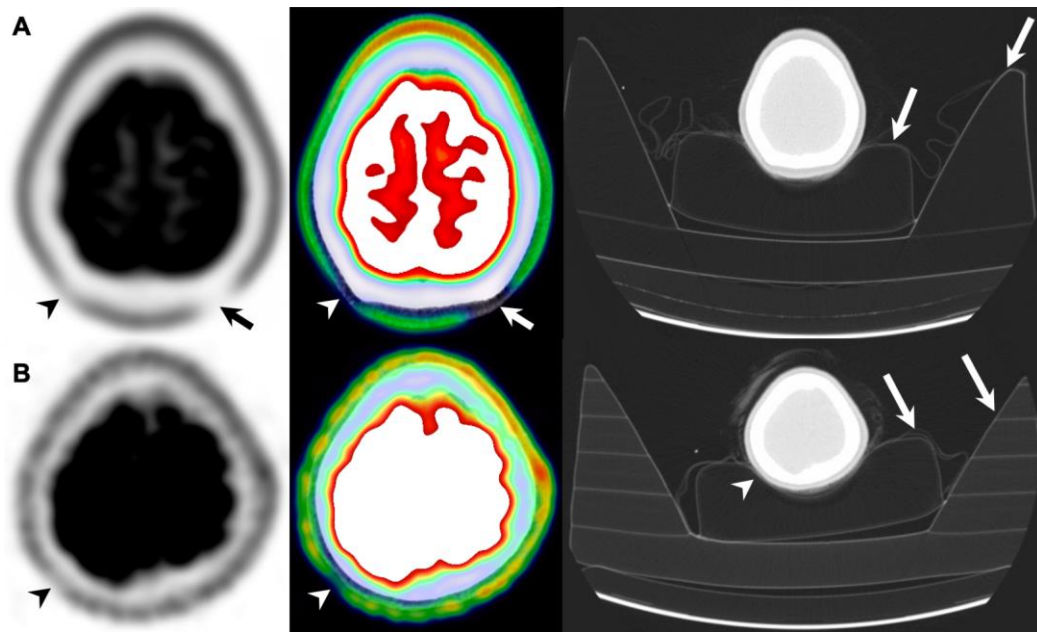
Example of complete (A) and partial (B) blanching defects. (A) Images from a 29-year-old healthy female, 81 kg, 165 cm, injected with ^{18}F-FDG (369 MBq). PET image (left) demonstrates bilateral posterior parieto-occipital scalp defects, complete on the left side (arrow) and partial on the right side (arrowhead). Fused ^{18}F-FDG PET/CT (middle) showed no CT abnormality. Lung window (right) outlines the head support setup (arrows). (B) images from a 43-year-old healthy female, 53 kg, 160 cm, injected with ^{18}F-FDG (18.5 MBq). PET image (left) demonstrates relative photopenia at the right posterior parietal scalp region (arrowhead), representing partial blanching defect. The contralateral (left side) shows no abnormality. Fused ^{18}F-FDG PET/CT (middle) showed no CT abnormality at the site of partial defect. Lung window (right) outlines the head position within the support setup (arrows) and demonstrates minimal tilting of the skull towards the side of the partial defect (arrowhead).

FIGURE 2:
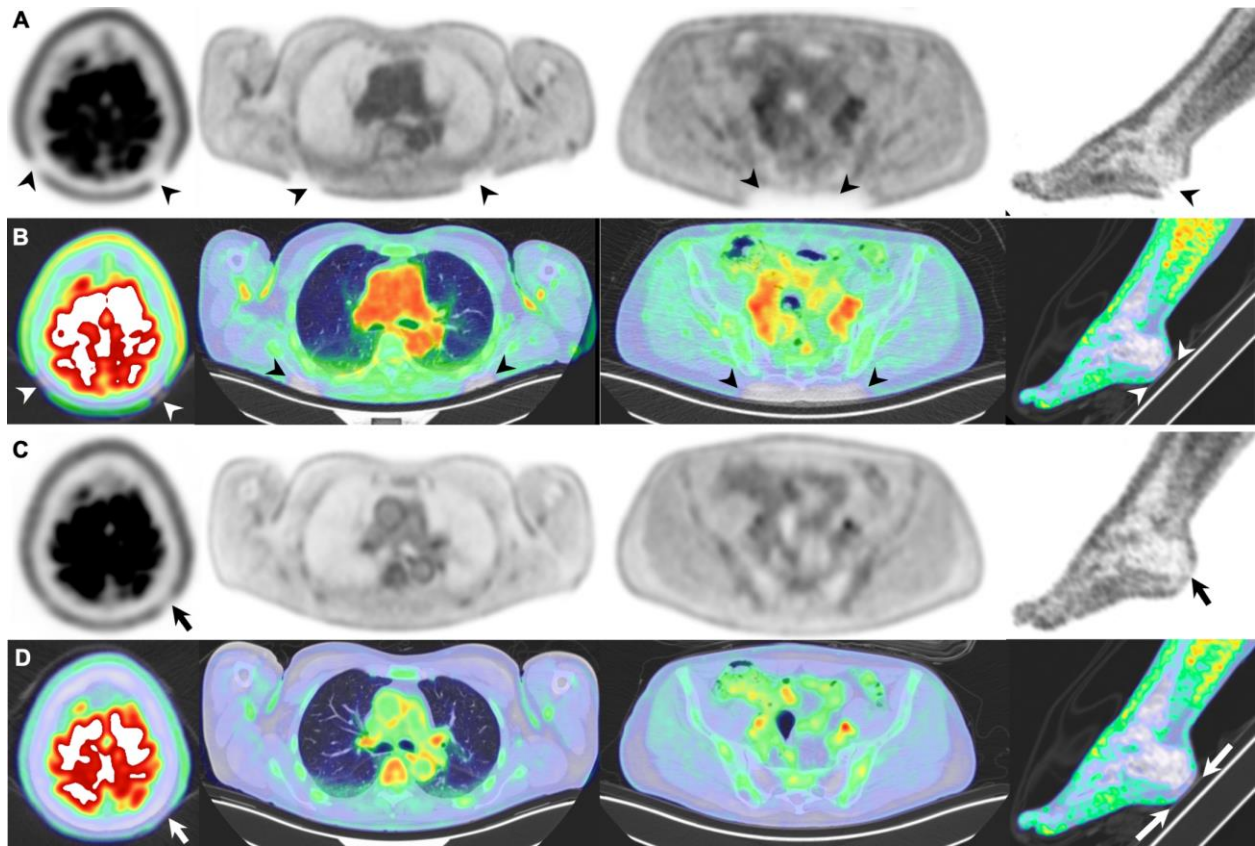
Examples of partial and complete restoration of uptake within complete blanching defects seen at the pressure points, from left to right, against the skull and scapulae bilaterally, sacrum, and left calcaneus. PET images from the last 20-min of a dynamic 60-min acquisition (A), their respective 20-min static acquisition at 90-min. (C), and the corresponding fused PET/CT images (B & D) in lung window; to demonstrate the relationship with the positioning setup and scanner table. Sites with complete defects on the dynamic images are marked with arrowheads while sites with partial restoration at 90-min timepoint are marked with arrows. The blanching defects against the skull showed complete restoration on the right side and partial restoration on the left side, those against

the scapulae and sacrum showed complete restoration, while the defects opposite the

heel showed partial restoration on delayed 90-min image.

FIGURE 3:
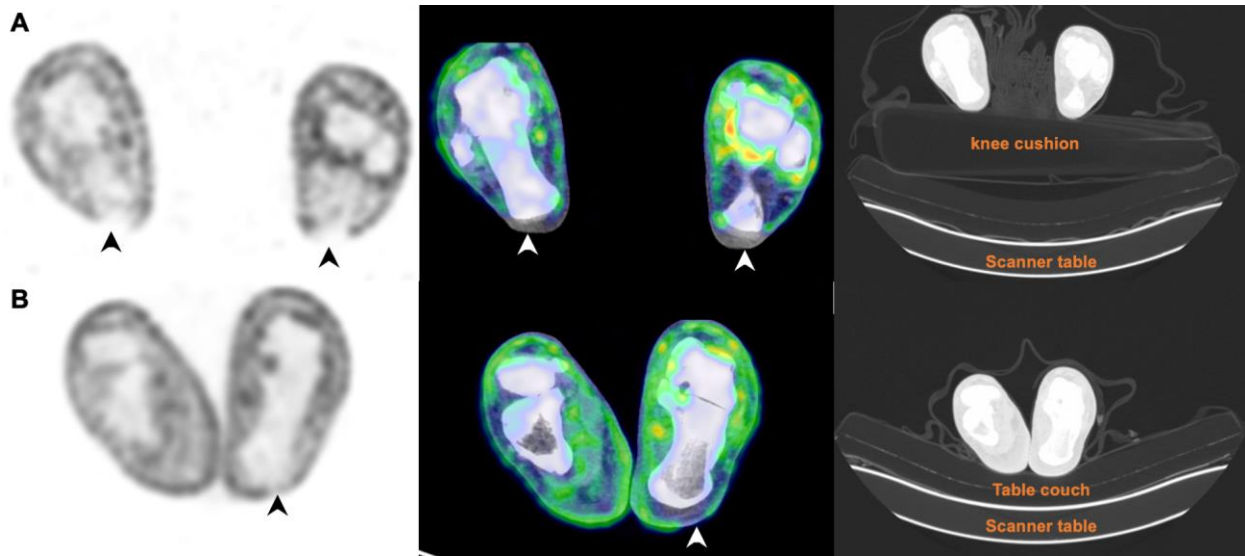
Changes in the pattern of blanching defects against the calcaneus in the same subject across two dynamic scans, baseline (A) and follow-up (B), separated by 2 weeks. Representative images from a male patient with GUC cancer, 74-year-old, 74 kg, 170 cm. ^{18}F-FDG PET images demonstrating bilateral complete blanching defects opposite the calcaneus (A, arrowheads) with no corresponding abnormality in the fused PET/CT image (middle). A follow-up dynamic PET scan in the same subject showed unilateral partial defect on the left foot (B, arrowhead). CT images with lung window (right) outlines the positioning setup demonstrating the relationship of the heels in respect to the knee cushion (top) and the table couch (bottom) during the respective scan timepoints.

FIGURE 4:
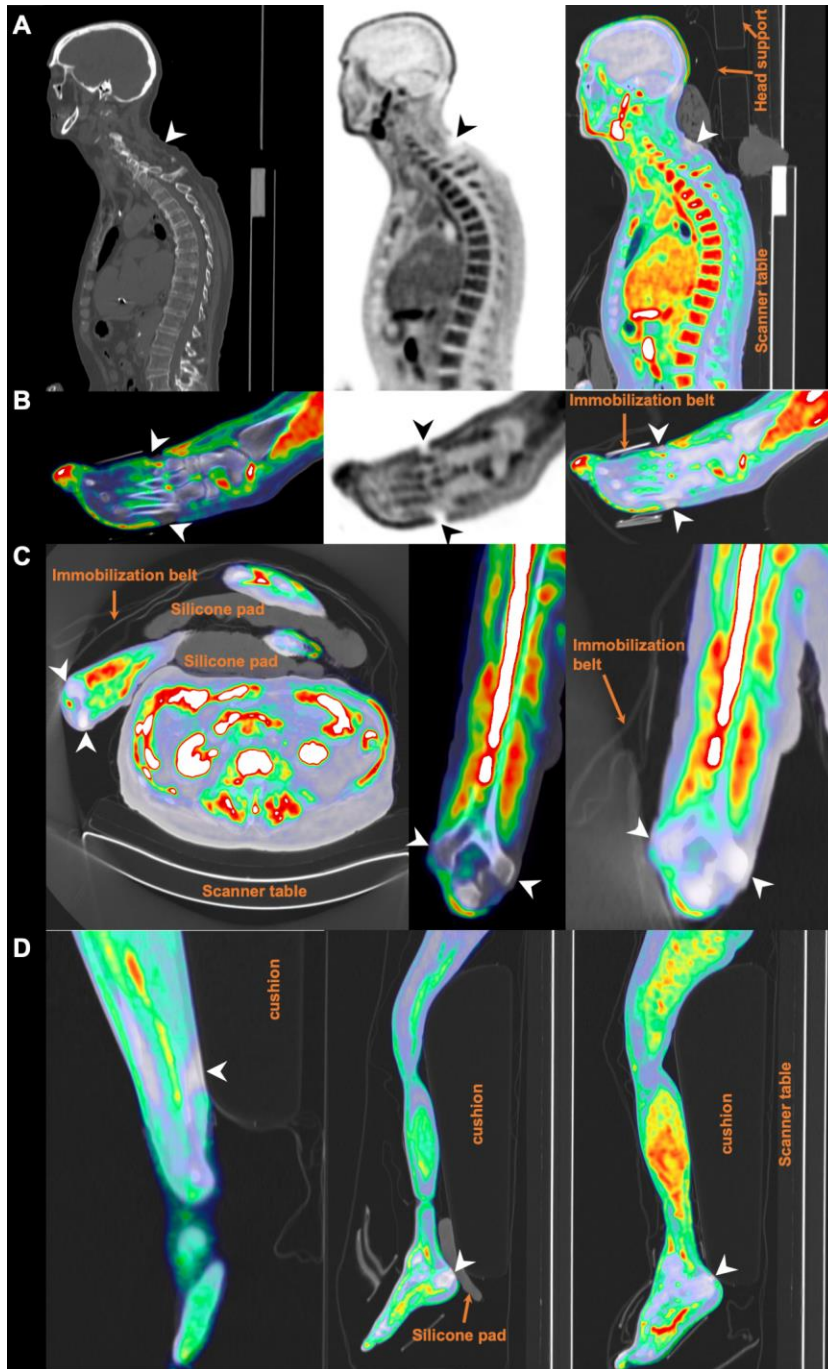
Examples of other non-systematic blanching defects (arrowheads). Absent

skin/subcutaneous ^{18}F-fluciclovine uptake opposite the cervico-dorsal vertebrae (A) at the

site of transition between the head support and the scanner table, which might be caused

by pressure against the prominent spinous processes; absent ^{18}F-FDG uptake at the dorsum of the foot (B) at the site of tightened immobilization belt; reduced-to-absent ^{18}F-fluciclovine uptake opposite the medial and lateral epicondyles of the right humerus (C) at the site of wrapped immobilization belt around the elbows; and few additional patterns of blanching defects in the lower limb (D): at the distal third of the calf as it is pressing against the end of knee cushion (left), opposite the calcaneus although a silicon pad was placed to minimize the pressure (middle), and again opposite the calcaneus at the end of knee/leg cushion, where the heels do not touch the scanner table (right).

Tables

TABLE 1: General Characteristics of the Study Participants

Characteristic / Injected dose group	FDG (N=47)			Fluciclovine
	Low dose	Intermediate dose	Standard dose	Standard dose
Age (yrs)	45±11.1 (26-62)	51.7±9.3 (39-66)	55.1±15 (26-78)	71.0±8.3 (54.1-89)
Weight (kg)	78.4±16.1 (53.1-102.5)	95±17.9 (77-131.7)	81.8±15.1 (53-113)	91.0±16.7 (68.4-148)
Height (cm)	173.6±10.5 (157.5-195.6)	170.6±12.4 (152.4-193)	171.1±8.3 (157.5-185.4)	178.1±7.8 (165.1-195.6)
BMI (kg/m^2)	25.8±3.4 (20.4-32.2)	32.6±4.5 (26.8-40.4)	28±5.3 (19.4-37)	28.7±5.4 (19.4-46.8)
Injected dose (MBq)	19.6±1.7 (17.2-23.5)	188.4±8.6 (175.7-196.7)	372.3±17.0 (331.9-393.8)	314.6±19.7 (287.2-389.6)
Fasting duration (Hrs)	9.2±3.0 (6-15)	11.4±3.4 (6-18)	11±2.9 (6-20)	6.9±3.4 (4-16)
Blood glucose (mg/dL)	90.7±19.2 (39-113)	94.3±12.7 (76-113)	97.9±21.8 (65-154)	N/A
Sex				
Female	7	2	9	0
Male	8	8	13	30
Disease				
Cancer	0	0	7	30
CVD	0	10	0	0
Healthy	15	0	15	0
Imaging timepoints				
Dynamic & delayed	15	10	15	0
Dynamic only	0	0	7	30
Arms position				
Above head	0	0	0	29
To the sides	15	10	22	1
AC CT dose				
Ultra-low-dose (5 mAs)	15	10	15	0
Low-dose (50 mAs)	0	0	7	30
Fused PET/CT misregistration				
No	10	8	17	25
Yes	5	2	5	5

TABLE 2: Kappa Agreement on Defect Detection/Laterality and Grade between the Two Readers according to the Scan Timepoint and the Evaluated Pressure Points

Scan timing & Evaluated pressure points	Agreement	
	Detection*	Grade of defect
Dynamic only	0.81 (0.75-0.88)	0.81 (0.75-0.83)
90-min only	0.66 (0.44-0.88)	0.70 (0.49-0.91)
Skull	0.76 (0.62-0.89)	0.75 (0.60-0.89)
Scapulae	0.84 (0.74-0.95)	0.88 (0.80-0.95)
Sacrum	0.72 (0.55-0.89)	0.74 (0.60-0.89)
Calcaneus	0.78 (0.66-0.90)	0.82 (0.73-0.92)

*Agreement figures on 'Detection' also include agreement on laterality.
Numbers in parentheses represent the 95% CI.

TABLE 3: Distribution of Blanching Defects according to the Anatomical Site, Laterality and Grade on Dynamic and Delayed Imaging

Imaging timepoint & site / Blanching defects	Dynamic (N=77 participants)				Delayed Static (N=40 participants)[*]			
	Skull	Scapulae	Sacrum	Calcaneus	Skull	Scapulae	Sacrum	Calcaneus
Absent	53	43	58	9	37	37	38	32
Present	24	34	19	47	3	3	2	6
One or unilateral								
Partial	8	2	8	1	1	2	2	3
Complete	5	3	11	7	0	0	0	0
Two or bilateral								
Partial	3	8	N/A	4	2	1	N/A	3
Complete[†]	8	21	N/A	35	0	0	N/A	0
Outside the FOV	0	0	0	*21*	0	0	0	*2*

37 out of the original 77 participants did not perform 90-min imaging
[†]*In the presence of bilateral defects with different defect grades, the higher grade was recorded for that pressure point. N/A=not applicable as the sacrum was evaluated as a single pressure point*

Graphical Abstract

Head support

Scanner table

Cushion
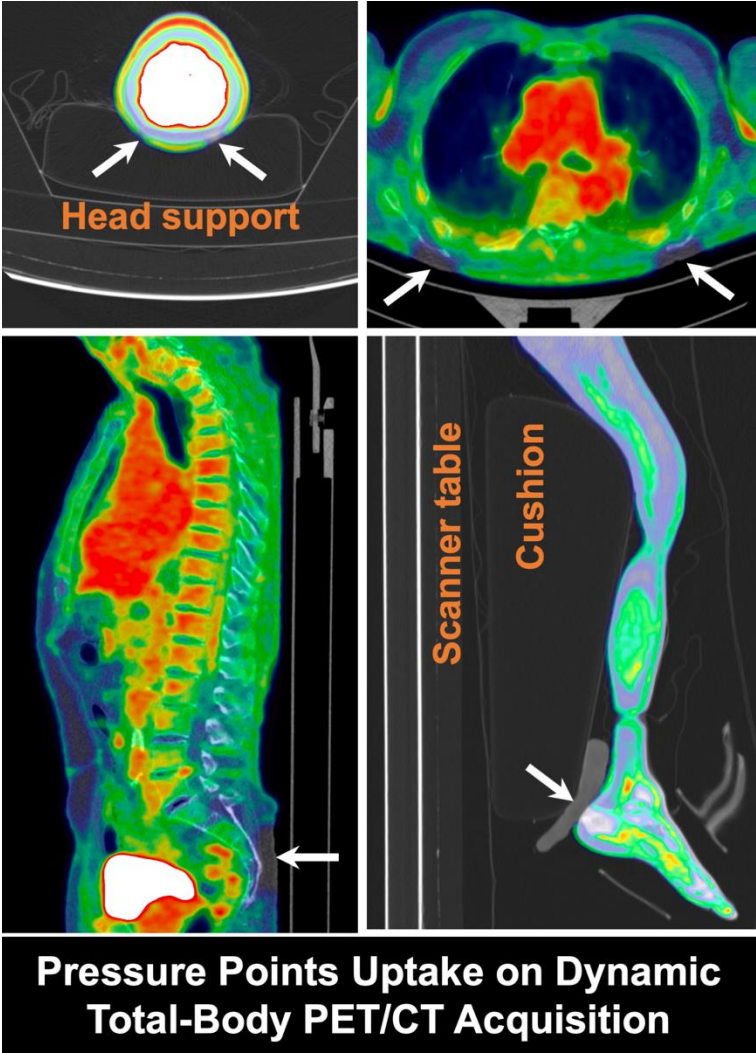
Pressure Points Uptake on Dynamic Total-Body PET/CT Acquisition

Supplementary TABLE S1: Characteristics Associated with Blanching Defects at Each Evaluated Pressure Point

Blanching defect site	Skull			Scapulae			Sacrum			Calcaneus		
Characteristic	**Absent**	**Present**	*P*	**Absent**	**Present**	*P*	**Absent**	**Present**	*P*	**Absent**	**Present**	*P*
Age (yrs)	56.2±14.7 (26-89)	64.8±14.5 (29-83)	0.019*	53.2±14.3 (26-83)	66.1±13 (26-89)	<0.0001*	56.8±15.3 (26-89)	65.1±13 (37-83)	0.037*	62.3±15.9 (30-83)	55.3±15.8 (26-89)	0.233
Weight (kg)	85.8±16.1 (53-131.7)	87.7±19.5 (53.1-148)	0.650	86.2±19.5 (53-148)	86.7±13.7 (59-119)	0.907	87.9±18.6 (53-148)	81.8±10.5 (68.4-102.5)	0.079	79.7±11.8 (57.8-101.2)	83.4±15.5 (53-113)	0.505
Height (cm)	173±10 (152-196)	176±10 (160-196)	0.200	171±10 (152-193)	178±8 (165-196)	0.002*	173±9 (152.4-193)	178±9 (163-196)	0.047*	173±6 (165-180)	171±9 (152-196)	0.514
BMI (kg/m²)	28.6±4.9 (19.4-40.4)	28.2±5.9 (19.4-46.8)	0.769	29.3±5.8 (19.4-46.8)	27.4±4.3 (19.4-36.6)	0.118	29.3±5.5 (19.4-46.8)	25.9±3.1 (19.4-31.1)	0.001*	26.7±3.5 (20-32)	28.7±5.2 (19.4-40.4)	0.277
Injected dose (MBq)	244±143 (17-394)	283±92 (18-370)	0.159	235±145 (17-394)	283±104 (19-392)	0.092	239±137 (17-394)	308±90 (21-390)	0.016*	251±144 (17-379)	239±143 (18-394)	0.829
Fasting duration (Hrs)	9.6±3.6 (4-20)	8.0±3.7 (4-16)	0.078	9.9±3.1 (4-18)	8.1±4.2 (4-20)	0.045*	9.1±3.8 (4-20)	9.1±3.4 (4-15)	0.999	9.3±3 (4-12)	9.7±3.7 (4-20)	0.805
Blood glucose (mg/dL)	94.1±20.5 (39-154)	99.5±5.8 (92-105)	0.531	94.1±19.9 (39-154)	97.6±17.6 (65-128)	0.614	94.3±20.6 (39-154)	96.8±14.3 (79-128)	0.720	105.3±30.9 (79-154)	92.4±16.9 (39-130)	0.325
Sex												
Female	15	3	0.156	17	1	<0.0001*	17	1	0.033*	2	16	0.688
Male	38	21		26	33		41	18		7	31	
BMI categories												
Normal	11	7	0.736	9	9	0.447	11	7	0.043*	3	11	0.342
Overweight	25	10		18	17		25	10		5	19	
Obese	17	7		16	8		22	2		1	17	
Disease												
Cancer	19	18	0.006*	11	26	<0.0001*	26	11	0.662	5	14	0.362
CVD	8	2		9	1		8	2		1	7	
Healthy	26	4		23	7		24	6		3	26	
Used tracer												

Blanching defect site	Skull			Scapulae			Sacrum			Calcaneus		
Characteristic	Absent	Present	P	Absent	Present	P	Absent	Present	P	Absent	Present	P
FDG	41	6	<0.0001*	37	10	<0.0001*	37	10	0.425	6	35	0.688
Fluciclovine	12	18		6	24		21	9		3	12	
Injected activity												
Low dose	13	2	0.160	11	4	0.009*	14	1	0.185	2	12	1.000
Intermediate dose	8	2		9	1		8	2		1	7	
Standard dose	32	20		23	29		36	16		6	28	
Arms position												
Above	11	18	<0.0001*	5	24	<0.0001*	20	9	0.414	3	12	0.688
Side	42	6		38	10		38	10		6	35	
AC CT Dose												
Ultra-Low-dose	34	6	0.003*	32	8	<0.0001*	32	8	0.429	4	33	0.247
Low-dose	19	18		11	26		26	11		5	14	
Fused PET/CT misregistration												
No	39	21	0.240	33	27	1.000	45	15	1.000	5	35	0.259
Yes	14	3		10	7		13	4		65	12	
Knee cushion												
No	3	0	0.548	2	1	1.000	2	1	1.000	1	2	0.415
Yes	50	24		41	33		56	18		8	45	
Back cushion												
No	49	24	0.304	40	33	0.626	54	19	0.567	8	45	0.259
Yes	4	0		3	1		4	0		1	2	

* Statistically significant